coatings

MDPI

Article

Synthesis, Microstructural, and Mechano-Tribological Properties of Self-Lubricating W-S-C(H) Thin Films Deposited by Different RF Magnetron Sputtering Procedures

Todor Vuchkov [1,2,*], Talha Bin Yaqub [1,2], Manuel Evaristo [2] and Albano Cavaleiro [1,2]

[1] IPN–LED & MAT—Instituto Pedro Nunes, Laboratory for Wear, Testing and Materials, Rua Pedro Nunes, 3030-199 Coimbra, Portugal; talha.yaqub@gmail.com (T.B.Y.); albano.cavaleiro@dem.uc.pt (A.C.)

[2] SEG-CEMMPRE, Department of Mechanical Engineering, University of Coimbra, Rua Luís Reis Santos, 3030-788 Coimbra, Portugal; manuel.evaristo@dem.uc.pt

* Correspondence: todor.vuchkov@ipn.pt; Tel.: +351-239700900

Received: 27 January 2020; Accepted: 9 March 2020; Published: 14 March 2020

Abstract: Carbon-alloyed transition metal dichalcogenide (TMD) coatings have great potential for providing a good tribological response in diverse operating environments. There are different ways to synthesize these coatings by magnetron sputtering, with no clear indication of the best possible route for potential upscaling. In this study, tungsten-sulfur-carbon (W-S-C) coatings were deposited by radio frequency (RF) magnetron sputtering via four different methods. All coatings were sub-stoichiometric in terms of the S/W ratio, with the bombardment of the growing film with backscattered Ar neutrals being the main mechanism governing the S/W ratio. The crystallinity of the films was dependent on the C and S contents. X-ray photoelectron spectroscopy (XPS) revealed W-S and W-C bonding in all coatings. Raman spectroscopy showed the presence of an a-C phase with predominant sp^2 bonding. The hardness of the coatings may be related to the C content and the S/W ratio. A friction coefficient of 0.06–0.08 was achieved during sliding in ambient air by the coatings deposited in non-reactive mode with optimal C contents. The results indicate that sputtering in non-reactive mode should be the method of choice for synthesis of these coatings.

Keywords: magnetron sputtering; transition metal dichalcogenides; tribology

1. Introduction

Tungsten disulfide (WS_2) is a well-known transition metal dichalcogenide (TMD) often used for tribological applications due to its lubricity. Its solid lubricant character is a result of its hexagonal crystal structure consisting of layers of transition metal (W) sheets sandwiched between two layers of chalcogen atoms (S). The bonding within the S-W-S sandwich is of the covalent type, while the sandwiches are held together by weak van der Waals forces. Because of the weak bonding between lattice layers, when shear forces are applied, interlamellar slip occurs resulting in easy sliding [1].

TMD materials have been used to improve the tribological behavior of different tribosystems. Some of the routes by which TMD materials are used include the following: coatings (thin films) [2], additives in oils [3], or tribochemically induced formation of TMD tribolayers [4]. Magnetron sputtering has often been a method of choice for deposition of TMD-based thin films because of its versatility.

The major drawbacks of pure sputtered TMD coatings are their low load-bearing capacity (related to their low hardness of 0.2–2 GPa) and sensitivity to oxygen, rendering these coatings unusable for tribological applications in terrestrial air environments. To enhance the tribological viability of these materials, doping with metals (Ti [5], Cr [6]) and non-metals (C, N [7,8]) during their synthesis by

physical vapor deposition (PVD) processes has often been attempted. Doping with metals (Ti) was successfully performed by Teer et al. [5]. In their study, titanium was co-sputtered with MoS_2, resulting in coatings with superior mechanical properties and significantly improved tribological performance as compared to pure sputtered MoS_2 coatings. Another successful improvement of the properties of sputtered MoS_2 coatings was reported by Scharf et al. [9]. The authors deposited a nanocomposite $MoS_2/Sb_2O_3/Au$ by a sputtering technique. The coatings showed good tribological performance in ambient air and dry N_2 environments.

Carbon addition is one of the most successful ways of making TMD materials feasible for tribological applications [10]. Voevodin et al. [2] deposited a nanocomposite WC/DLC/WS_2 thin film, which consisted of nanograins of WC and WS_2 of 5–10 nm embedded in an a-C matrix, by pulsed laser deposition. The nanocomposite coating had adaptive tribological behavior related to the testing atmosphere, with WS_2 governing the friction in inert (i.e., vacuum and dry N_2) environments, while C-based tribofilms were responsible for friction reduction in humid ambient air environments. The results presented in the study by Voevodin et al. cannot be achieved with the more conventional coatings of the metal carbide/DLC type (e.g., WC/DLC or TiC/DLC). The main issue regarding the metal carbide/DLC type coatings is their inability to provide friction and wear in a vacuum. This is due to the friction-induced graphitization of the carbon phase. Graphite needs an intercalating agent (for example, water molecules) in order to be an efficient solid lubricant, and hence these films perform well only in humid ambient air environments [11]. On the other hand, TMD compounds perform exceptionally well in a vacuum, and nanocomposite TMD-C coatings with optimized structural and mechanical properties can provide low friction and wear in a wide range of sliding environments (from high vacuum to humid ambient air conditions). Further studies on C-doped TMD films (~50% C) were performed by Polcar and Cavaleiro [10,12], where friction coefficients as low as 0.05 were reported while dry sliding in humid environments against steel counterbodies. The tribological response of these films was mainly governed by TMD tribofilms present on the sliding interface, with the C phase being responsible for the hardness improvement and the protection of the TMD platelets from environmental attack. The films were generally deposited using radio frequency (RF) magnetron sputtering equipment by different routes (co-sputtering of two targets and sputtering of a composite target). The films deposited by these different routes were studied in a time span of several years, and it is still not clear which is the best route for potential upscaling. A recent study performed on W-S-C(H) coatings [13] has shown that co-sputtered hydrogen-free coatings display the best tribological performance, with evidence that the C phase plays a role in the frictional response during sliding in ambient air conditions, contrary to the studies done by Polcar and Cavaleiro.

A major issue regarding the synthesis of TMD-containing thin films by way of magnetron sputtering is the sub-stoichiometry in relation to the S/M ratio (M—transition metal, S—chalcogen atom), which is often much lower than the stoichiometric value of 2. The sub-stoichiometry has a strong effect on the tribological properties and the hardness of the films. Different routes of deposition result in various chemical compositions of the films, with S/M ratios in the range of 0.8–1.7 [14,15]. Previous studies on W-S-C films have shown that some deposition methods, such as reactive sputtering in methane (CH_4) gas [16], led to very poor stoichiometry (<1) compared to films deposited by co-sputtering of graphite and WS_2 targets, where values between 1.5 and 1.8 have been achieved [14]. The mechanisms behind the variation in the S/M ratio are poorly understood. The main mechanisms considered are the different scattering behaviors of the sputtered species during their travel from the target towards the substrates and the preferential resputtering of the chalcogen atoms from the growing film due to bombardment with energetic Ar neutrals. Furthermore, sputtering in a reactive gas containing hydrogen (e.g., methane) might lead to the formation of hydrogen sulfide gas and subsequent pump-out.

Nanocomposite coatings of the TMD-C type can have unique tribological properties. The literature reports synthesis of this type of coatings by different PVD-based methods such as pulsed laser deposition or magnetron sputtering. In both these methods, deposition can be further performed by using a

composite target (e.g., a graphite target with WS_2 segments placed on it), two separate targets of graphite and WS_2, or sputtering a WS_2 target in a hydrocarbon-containing gas. Depending on the deposition method, the S/W ratio can significantly vary, strongly affecting the properties of the coatings. There is generally a lack of information regarding the relationship between the different deposition procedures and the properties of the coatings. Therefore, there is no clear indication of the best route for synthesis of these coatings by magnetron sputtering. In this study, we aim to reach a better understanding of how the deposition method affects the composition, microstructure and mechanical properties of W-S-C (H) deposited by magnetron sputtering. For this purpose, we deposited coatings by RF magnetron sputtering using four different procedures. Numerous relevant properties such as the composition, morphology, crystallinity, chemical bonding, hardness, adhesion, and tribological properties were studied and discussed as a function of the deposition procedure. The relationships established by this systematic study can be ultimately used for proper selection and upscaling of the deposition process to a bigger deposition unit.

2. Materials and Methods

2.1. Deposition of W-S-C-(H) Coatings

Depositions were performed by RF magnetron sputtering using Edwards E306A equipment (Edwards Vacuum, Burgess Hill, UK). A schematic of the deposition setup can be seen in Figure 1.

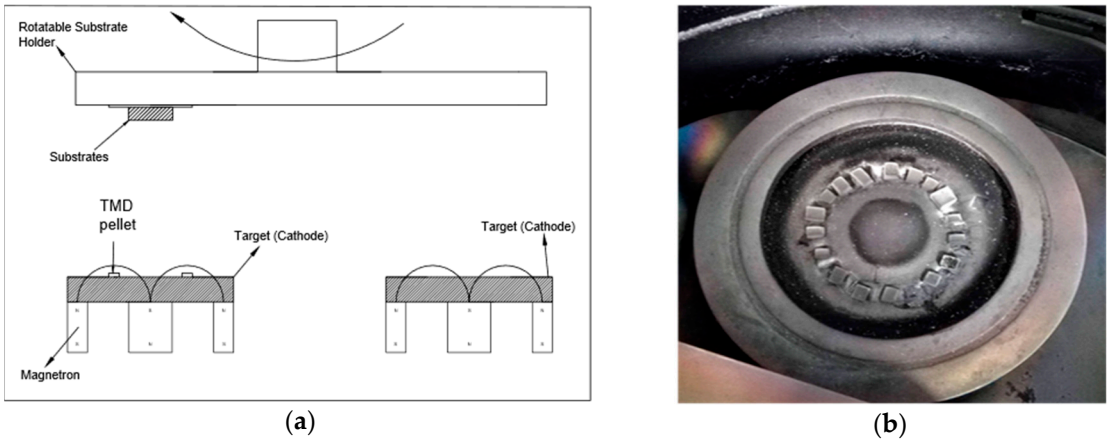

Figure 1. (**a**) Schematic of the RF magnetron sputtering unit; (**b**) carbon target with WS_2 pellets placed in the erosion zone.

The chamber is equipped with 2 cathodes with a diameter of 100 mm powered by RF (13.56 MHz) power supplies. The substrate is also connected to an RF power supply for biasing during deposition, and sputter cleaning before deposition. The base pressure before deposition was less than 10^{-3} Pa, attained by a turbomolecular pump backed by a rotary vane vacuum pump. The distance between the targets and the rotatable substrate holder was fixed at 6 cm. Depositions were carried out using Ar gas with a pressure of 0.75 Pa, except for the reactive sputtering where a gas mixture of Ar/CH_4 with a total pressure of 1 Pa was used.

Co-sputtered films were deposited by sputtering separate WS_2 and C targets. The power density to the WS_2 target was set to 2 W/cm^2, while the power to the C target was varied between 3.8 W/cm^2 and 7.6 W/cm^2 (300–600 W) in order to deposit films with C contents between 40% and 50% as these compositions showed the best tribological results in previous studies. The films deposited by sputtering a composite target were prepared by placing WS_2 pellets (5 mm × 4 mm × 2 mm) in the erosion zone of the C target. To obtain similar C contents to the co-sputtered coatings, the number of pellets was changed between 21 and 13. In this particular case, thin films were deposited by having the substrate holder rotating or in stationary position because the equipment has the possibility of placing the

substrate holder directly on top of one of the targets. The number of pellets was kept the same for both modes. The power density was set to 7.6 W/cm^2 and 3.8 W/cm^2 for the rotating and stationary modes, respectively. Magnetron sputtering in reactive mode was done by sputtering a WS_2 target in a gas mixture of Ar and methane (CH_4). In this case, depositions were performed only by having the substrate holder rotating. The power density used was 3.8 W/cm^2. The partial pressure of the CH_4 gas (p_{CH4}/p_{total}) was set to 28%–48% by adjusting the flow of the CH_4 gas.

Three films were deposited per route, resulting in total of 12 films. The coatings are referred to as Dx-y, where x = 1, 2, 3, 4 refers to: 1—co-sputtering of 2 targets; 2—sputtering a composite target with the substrate rotating; 3—sputtering a composite target with the substrate being stationary; and 4—reactive sputtering. The number y refers to the power (W) to the C target used for the co-sputtered films, number of pellets for the sputtering of a composite target, or partial pressure (%) of the CH_4 gas during reactive sputtering. For example, D3-17 is the film deposited by sputtering a composite target with 17 pellets placed in the erosion zone and a stationary substrate holder. Before deposition, the targets were sputter-cleaned for 10 minutes each, while the substrates were sputter-cleaned for 20 min. For improving the adhesion to the metallic substrates, a Cr interlayer with a thickness of ~200 nm was deposited for the films deposited by sputtering a composite target and by reactive sputtering (D2, D3 and D4 coatings). For the D1 case, a Cr interlayer could not be deposited as both cathodes were used for the deposition of W-S-C coatings. The substrates used were silicon wafers and AISI M2 steel coupons. Steel substrates were polished to Ra~20 nm using a diamond suspension, and they were mainly used for the scratch testing and tribological evaluation. The substrates were not biased during deposition, and no intentional substrate heating was used.

2.2. Characterization of the Coatings

Fractured cross-sections allowed for microstructural characterization and thickness measurement by using a field emission scanning electron microscope (FESEM Zeiss Merlin, Oberkochen, Germany). The chemical composition was assessed using wavelength dispersive spectroscopy (WDS, Oxford Instruments, High Wycombe, UK). The crystallinity of the coatings was studied using grazing incidence X-ray diffraction (GIXRD). The investigation was performed using a PANalytical X'pert MRD diffractometer (PANalytical B.V., Almelo, Netherlands)) and using Cu Kα radiation. Chemical bonding was assessed using X-ray photoelectron spectroscopy (Kratos Axis Ultra HAS, Manchester, UK) with monochromatic Al Kα X-rays (hν = 1486.6 eV). The power of the X-ray source was set to 90W, and a charge neutralizer was used during the acquisition. Survey spectra were obtained by setting the pass energy at 80 eV, with a step of 1 eV and a dwell time of 200 ms. The high-resolution spectra of the regions of interest were obtained using a pass energy of 40 eV, with a step of 0.1 eV and a dwell time of 600 ms. Sputter etching was performed for 10 min using an Ar ion gun operated at 2.2 keV and a current density of 2.2 μA/cm^2. The data acquisition was performed at pressures lower than 10^{-6} Pa. Because of the presence of C in the films, charge correction for the binding energies was performed using the oxygen O1s peak (BE = 530.6 ± 0.1 eV) from the high-resolution oxygen spectrum. Data fitting was performed using the CasaXPS software (version number 2.3.15). The baselines of the spectra were achieved using the Shirley method, and peak fitting was applied with Gaussian–Lorentzian functions.

The hardness of the coatings was assessed by nanoindentation (NanoTest, Micromaterials, Wrexham, UK) using a Berkovich tip. The load was adjusted to reach indentation depths of less than 10% of the thickness of the films in order to minimize the effects of the substrate. The film adhesion was assessed using scratch testing (CSM Revetest, Peseux, Switzerland). A Rockwell C indenter with a radius of 0.2 mm was used with the scratch speed set to 10 mm/min and a loading rate of 100 N/min. The load range selected for the scratch testing was from 5 to 40 N. The critical load (Lc) was evaluated by observing the scratch scars under a light microscope (Leica DM4000 M LED, Wetzlar, Germany). Tribological studies of selected coatings were performed using a unidirectional pin-on-disk apparatus in dry sliding conditions, in a laboratory air environment (RH = 30%–40%). Bearing steel (100Cr6) balls with a diameter of 10 mm were used as counterbodies, tests were performed under a load of 10 N

with a speed of 0.1 m/s, and the duration of the tests was limited to 2500 cycles. The wear volume of the disks was evaluated using a 2D profilometer (Mahr Perthometer S4P, Göttingen, Germany) with an optical head (Focodyn). Four profiles were acquired from four different areas across the circumference of the wear track. The wear volume was subsequently calculated by multiplying the cross-sectional area under the 2D profile with the circumference of the wear track. The wear of the counterbodies was assessed using an optical 3D profilometer (Alicona Infinite Focus, Graz, Austria). The volume of the wear scar was considered to be a spherical cap and calculated using the following expression:

$$V = \left(\frac{\pi h}{6}\right)\left(\frac{3d^2}{4} + h^2\right) \quad (1)$$

where h is the height of the cap, calculated as:

$$h = r - \sqrt{r^2 - \frac{d^2}{4}} \quad (2)$$

The scar diameter d is obtained from the 3D optical profilometer, and r is the radius of the ball (5 mm). Using the wear volumes, the specific wear rate was calculated (Equation (3)).

$$W_r = \frac{V}{Fs} \quad (3)$$

where F is the normal load and s is the sliding distance. At least two repetitions of the tribological tests were performed per coating tested.

3. Results and Discussion

3.1. Microstructure, Chemical Composition, and Crystallinity

The elemental composition of the deposited films can be seen in Table 1. The hydrogen content of the reactive sputtered films was not considered; the results presented for the hydrogenated coatings show the sum of C, W, S and O being 100 at.%. Changing the power applied to the carbon target, the number of pellets used, or the partial pressure of the CH_4 gas clearly affected the C contents of the coatings. The oxygen content is up to 12 at.%, and the highest values for the co-sputtered coatings are probably a result of the target contamination, residual oxygen present in the chamber, and longer deposition times (3 h compared to 1–2 h used for the other methods).

Table 1. Chemical composition, thickness, and deposition rate of the deposited coatings.

Type of Coating	Chemical Composition (at.%)				S/W Ratio	Thickness (μm)	Deposition Rate (nm/min)
	C	S	W	O			
D1-300W	37.6 ± 0.2	31.4 ± 0.3	19 ± 0.2	12 ± 0.3	1.62	1.6	9
D1-450W	42.5 ± 0.4	29.5 ± 0.1	20 ± 0.2	8 ± 0.2	1.48	1.4	7
D1-600W	47.1 ± 0.1	26.9 ± 0.6	16 ± 0.1	10 ± 0.1	1.68	1.9	11
D2-21p	22 ± 0.1	47 ± 0.1	26.9 ± 0.2	4.1 ± 0.1	1.74	2.8	24
D2-17p	25.5 ± 0.1	44.8 ± 0.3	26.3 ± 0.1	3.4 ± 0.1	1.72	2.6	22
D2-13p	34.4 ± 0.1	37.6 ± 0.5	24.5 ± 0.1	3.5 ± 0.3	1.54	2.2	18
D3-21p	31.3 ± 0.7	37 ± 0.4	26 ± 0.5	5.7 ± 0.1	1.42	1.6	27
D3-17p	38.5 ± 0.3	31.4 ± 0.1	25 ± 0.2	5.1 ± 0.1	1.25	1	17
D3-13p	49 ± 0.3	22.9 ± 0.1	23.3 ± 0.1	4.8 ± 0.2	0.98	0.7	12
D4-28%	47.9 ± 0.1	28 ± 0.1	18.8 ± 0.6	5.3 ± 0.2	1.50	0.5	8
D4-38%	51.4 ± 0.1	24.9 ± 0.2	19.1 ± 0.1	4.6 ± 0.3	1.30	1.1	9
D4-48%	58.8 ± 0.3	19.5 ± 0.1	15.8 ± 0.1	5.9 ± 0.5	1.23	0.7	11

The sulfur to tungsten ratio is of great importance in these films as it can affect the tribological performance [17]. The values (1.6–1.7) for the co-sputtered coatings are in agreement with previous

studies performed on co-sputtered W-S-C coatings deposited using the same equipment [14]. The S/W ratio for the coatings deposited by sputtering a composite target ranges between 1 and 1.7, depending on whether the deposition is carried out in stationary or intermittent mode. Reactive sputtered films (D4) also seem to be poorly stoichiometric, with values between 1.23 and 1.5.

Three mechanisms are generally cited for understanding the compositional variations obtained during magnetron sputtering of TMDs:

- Different scattering behaviors of sputtered atoms during their travel towards the substrate [18];
- Preferential re-sputtering of the sulfur atoms from the growing film as a result of energetic particle bombardment [16];
- Reaction of the sputtered species with the process gas and subsequent pump-out [14].

A significant S deficiency can be observed for the D3 and D4 families of coatings. The low S/W ratio observed for these coatings is, very likely, due to both the difference in scattering behavior as well as bombardment with backscattered Ar neutrals. The sputtered species, C, S, and W in this case, will have different scattering behaviors during their travel towards the substrates. The lighter elements, C and S, will be deflected to a greater extent as a result of collision with the Ar gas present in the chamber. The W atoms, which are much heavier, will have straight traversing paths towards the substrates. In this context, it is expected that the D2 coatings will be richer in the lighter elements, as the probability of arrival of the species that scatter more will be higher when the substrate holder is rotating. On one hand, this was observed for S, as the S/W ratio was higher for the D2 coatings compared to the D3 coatings. On the other hand, the C content was lower, indicating that the mechanism of preferential re-sputtering should also be considered. The energy of the backscattered Ar neutrals is proportional to the target voltage. The target voltage for the D2 coatings was higher (~800 V) compared to the D3 ones (~500 V), indicating that the energy of the backscattered Ar neutrals will be higher in the D2 case. Although the energy of the backscattered Ar neutrals is higher for the D2 coatings, these coatings still had a higher S/W ratio. Considering the lower S/W ratio and higher carbon content of the D3 coatings, it is very likely that these coatings are subjected to a higher flux of backscattered Ar neutrals with high energy. One of the parameters that should also be considered in this case is the substrate location. As the target-to-substrate distance is constantly changing for the D2 case, when the substrates are further away from the target there will be arrival of the lighter sputtered species that scatter more in the chamber (C and S), while the energetic argon neutrals will have significantly lower energy due to an increased number of collisions. In this context, it is expected that D2 coatings will have higher S contents. The increased carbon content for the D3 coatings is very likely because of the lower sputtering yield of carbon.

The lower S/W ratio for the D4 coatings (deposited in reactive mode) may be further caused by reaction of the sputtered S atoms with the H present in the chamber, and formation of H_2S gas and subsequent pump-out. The bombardment with backscattered Ar neutrals will also be amplified as the introduction of the reactive gas causes target poisoning, evident from the observed increase in the target voltage. The target voltage values varied between 1100 and 1200 V, with an increase with increased partial pressure of methane. This increase in target voltage will result in the generation of backscattered Ar neutrals with much higher energy.

Cross-sectional and top-view SEM micrographs for selected thin films are shown in Figure 2. The films generally have a compact morphology. Some porosity and signs of columnar growth can be observed for the D2-17 coating, which has a rather low amount of C (26 at.%). All the other cross-sectional micrographs present compact and featureless morphologies. Top-view micrographs show cauliflower-like structures. This morphology is typical for films deposited by magnetron sputtering under the influence of the atomic shadowing effect. It should be mentioned that the cauliflower features were not clearly evident for the coating deposited in reactive mode (see Figure 2h), and the micrographs revealed a smoother morphology. The smoothening is very likely due to the increased bombardment of the growing film with reflected Ar neutrals, since the energy (proportional to the target voltage) of the backscattered Ar neutrals was

the highest in this case. Bombardment of the growing film with energetic species increases the adatom mobility and thus reduces the atomic shadowing effect [19].

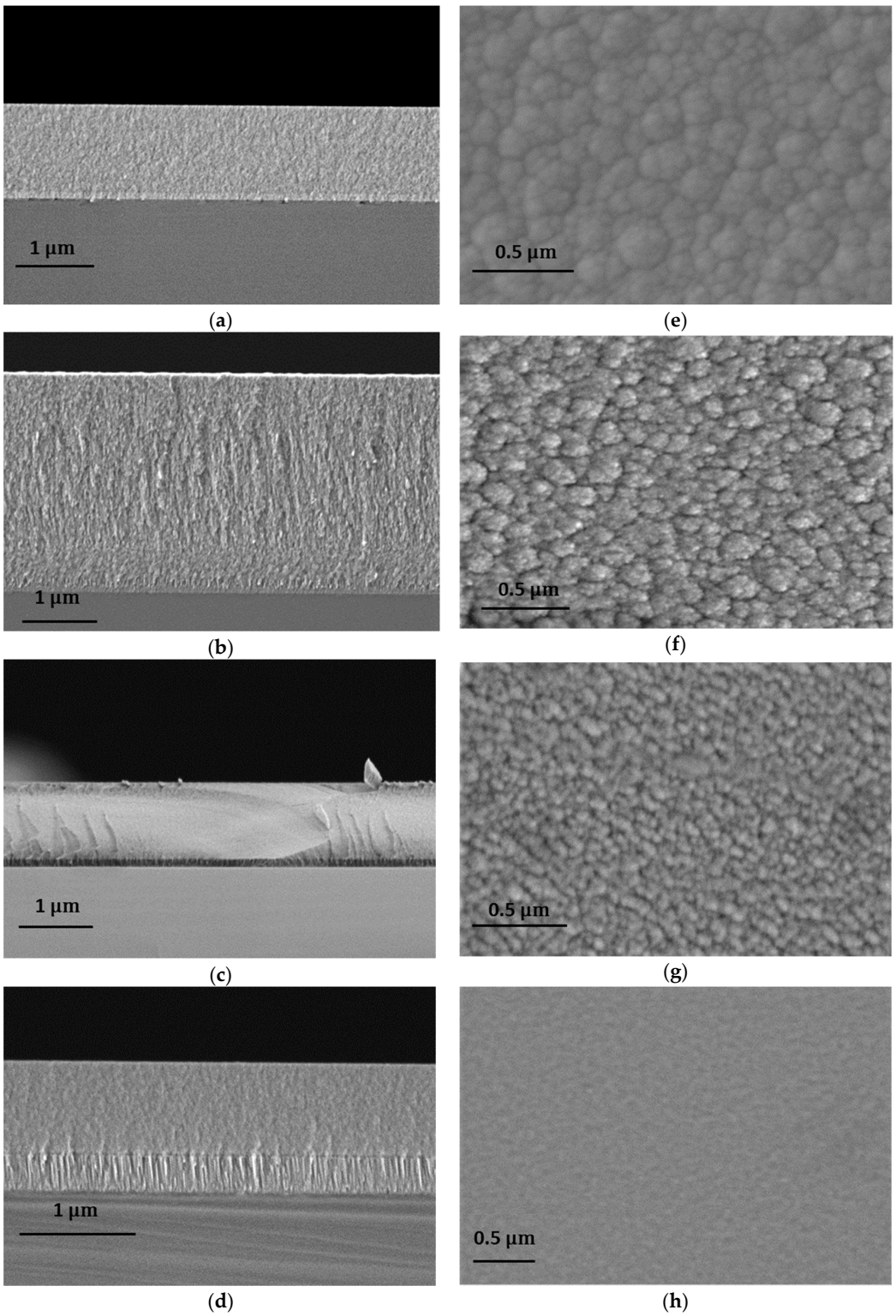

Figure 2. Cross-sectional SEM micrographs of: (**a**) D1-450; (**b**) D2-17; (**c**) D3-17; (**d**) D4-38; and their respective top-surface morphologies (**e**) D1-450; (**f**) D2-17; (**g**) D3-17; (**h**) D4-38.

GIXRD results are shown in Figure 3. Common for all patterns is the presence of a broad peak starting at 2θ~33°, which is associated with the (100) peak of WS_2 (ICDD card no. 00-008-0237), with a

tail towards higher angles representing a turbostratic stacking of the (10l) family of WS_2 planes with l = 1.2.3 [20]. Only the D2 films with low carbon contents have a sharper (100) peak and an additional (110) peak at 2θ = 59°. A small contribution of the (20l) family of planes with l = 0, 1, 2, 3 at 2θ~70° was also detected for these coatings. The small (002) reflection from the WS_2 phase (representing the basal planes parallel to the substrate) at 2θ~14° can only be seen on the pattern obtained for the D2-21 film. The Cr peak observed in the D3 and D4 films stems from the interlayer. The presence of tungsten carbides is difficult to detect from the XRD patterns as there are several W_2C- and WC_{1-x}- related peaks in the region of 2θ = 34.5–39° (ICDD card numbers: 00-035-0776, 00-020-1316) overlapping with the (10l) family of planes for WS_2. Some of the peaks often observed for magnetron-sputtered WC/a-C films are W_2C (100) at 2θ = 34.5°, W_2C (002) at 2θ = 38°, and WC_{1-x} at 2θ = 37° (see ref. [21,22]), with the authors of these previous studies reporting a broad peak in the range of 2θ = 34.5–39°.

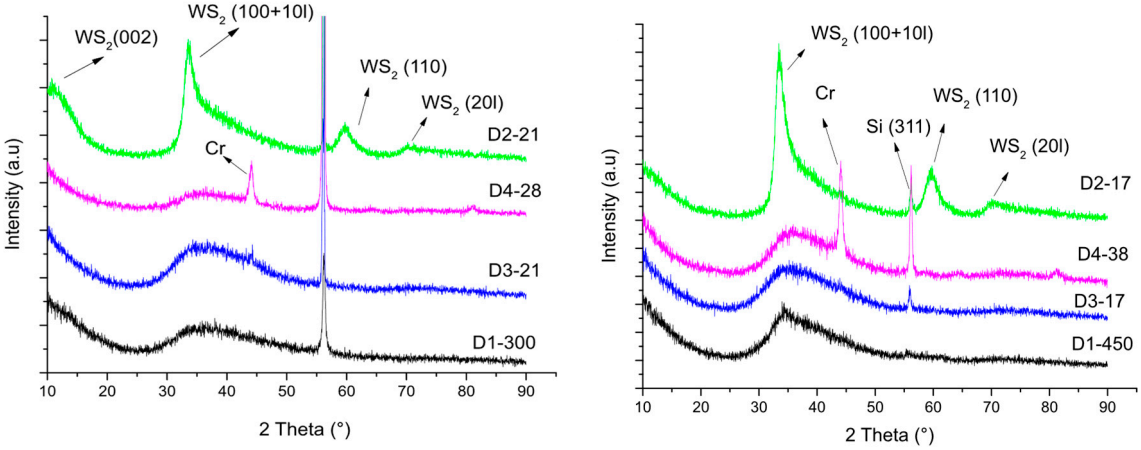

Figure 3. Grazing incidence X-ray diffraction (GIXRD) diffractograms for the coatings deposited by each deposition route: (**a**) lowest C content; (**b**) intermediate C content.

3.2. Chemical Bonding and Raman Spectroscopy

To reach a better understanding of the chemical bonding in the coatings, XPS and Raman spectroscopy (Horiba XploRA, Longjumeau, France) were performed on selected coatings from every deposition route. The spectra from the carbon region of interest, after sputter cleaning of the samples, are shown in Figure 4. Spectra before etching (not shown) generally consisted of a main carbon peak at a binding energy (BE) of 284.5 eV, which was identified as a C-C bond originating from the presence of adventitious carbon. The presence of adventitious carbon was confirmed by the presence of C-O bonds at a BE of 286 eV and C=O bonds at 288 eV. A small contribution from C-W bonding was also observed at the typical location of ~283–283.3 eV [23]. Fitting of the spectra obtained after etching (see Figure 4) was performed using two peaks, except for the spectrum obtained for the D4-48 coating, for which an additional peak was added at a higher binding energy to complete the fitting, which was identified as C-O bonding. Fitting was constrained by setting the maximum values of the full width at half maximum (FWHM) to 1.2 eV, with the location of the C-C bonding originating from the a-C phase being positioned at a BE location higher than 284.4 eV, and with the C-W bonding set to a BE location lower than 283.3 eV [21,22]. This fitting procedure resulted in a residual standard deviation of less than 1.5. Bonding of the C-W type was observed for all coatings. A major trend observed in the spectra is the dominance of the C-W bonding type for the coatings with low amounts of C (e.g., D2, D3-21). Increasing the C contents of the coatings results in larger areas for the peak related to C-C bonding (e.g., D1-450, D4-38), indicating the existence of increasing amounts of a-C. These trends were also observed for WC/C [21] and TMD-C [7] coatings in previous studies.

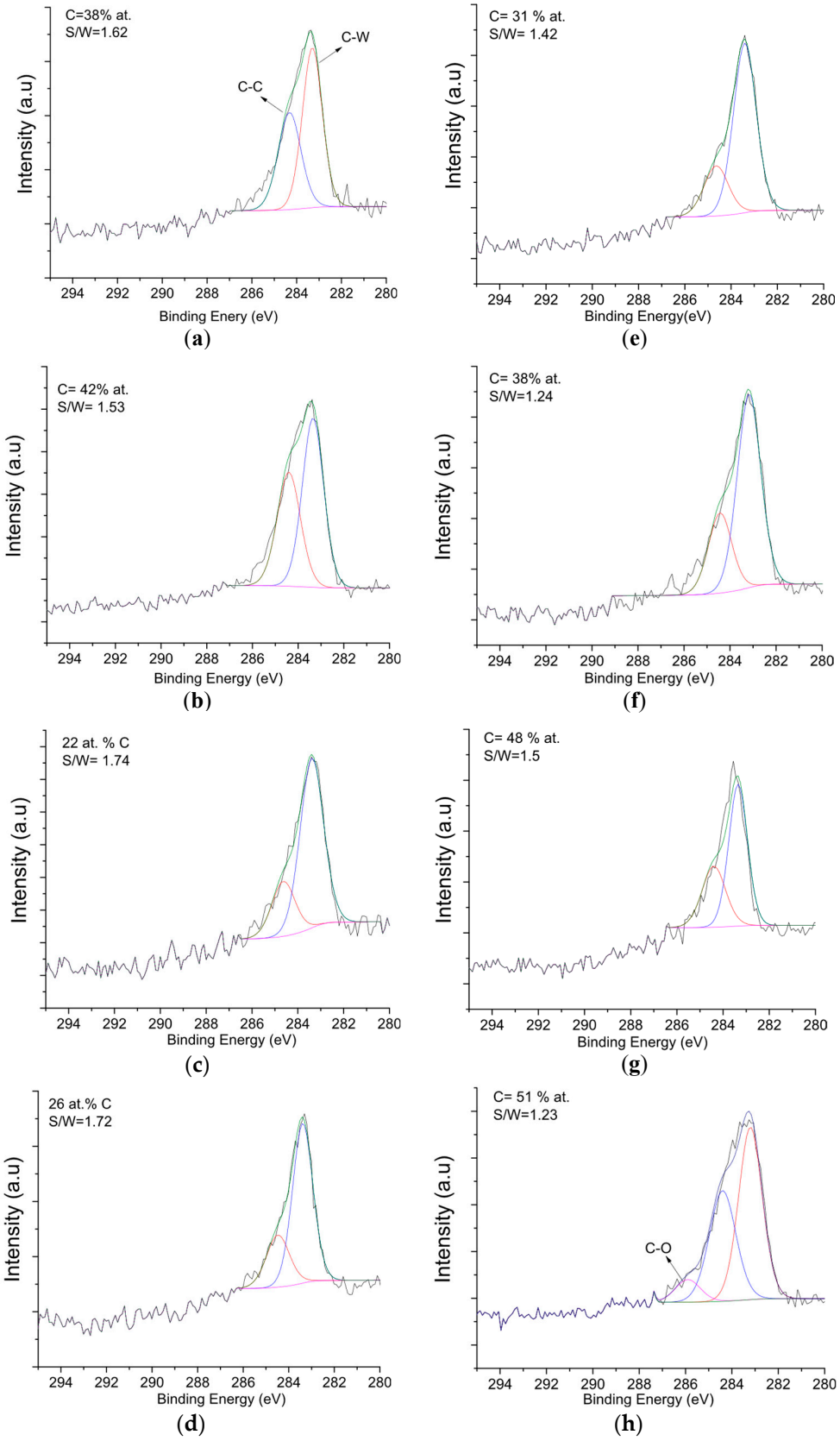

Figure 4. XPS spectra acquired in the C1s region of interest after sputter cleaning: (**a**) D1-300; (**b**) D1-450; (**c**) D2-21; (**d**) D2-17; (**e**) D3-21; (**f**) D3-21; (**g**) D4-28; (**h**) D4-38.

The spectra acquired from the W4f region of interest can be seen in Figure 5. The spectra obtained before sputter cleaning were quite similar, and only one is shown as a reference (Figure 5a). For the spectra obtained after sputter cleaning, a representative spectrum obtained from a coating deposited by each deposition route is shown in each case. Spectra acquired before sputter cleaning of the samples show strong features at higher binding energies, indicating the presence of tungsten oxides. The fitting was performed by setting the separation between the energy of the $W4f_{7/2}$-$W4f_{5/2}$ doublet to 2.18 eV, with the peak area ratios between $W4f_{7/2}$ and $W4f_{5/2}$ peaks set to 4:3 [24]. A total of four doublets were used to fit the spectra acquired before sputter cleaning.

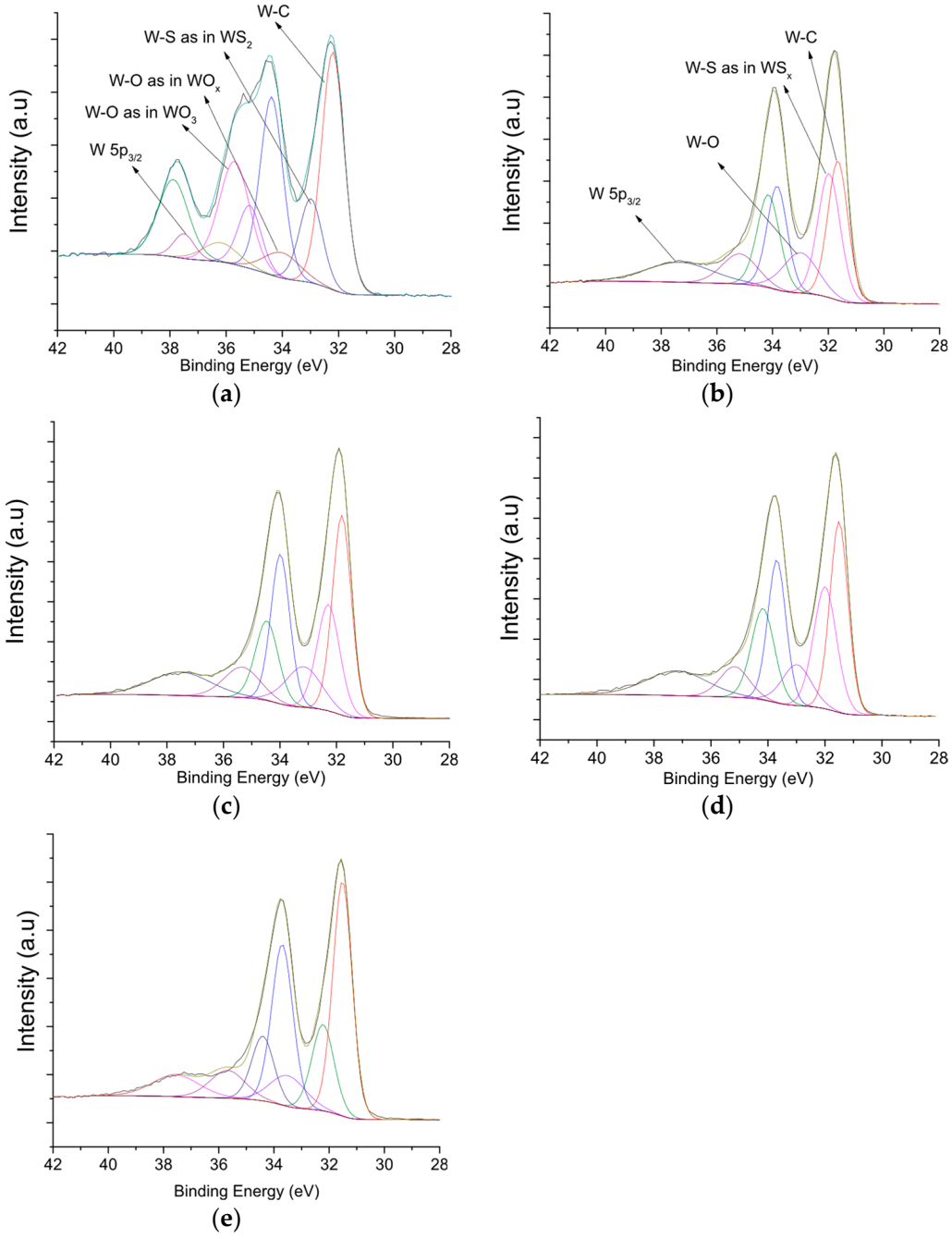

Figure 5. XPS spectra obtained in the W4f region of interest: (**a**) D1-450 before etching; (**b**) D1-450 after etching; (**c**) D2-17 after etching; (**d**) D3-17 after etching; (**e**) D4-38 after etching.

The location of the doublets is further indicated by the location of the $W4f_{7/2}$ peak. The location of the first doublet is at a BE of 32 ± 0.1 eV for all coatings, a location which is lower than the typical location

of W-S bonding in WS_2 often reported at 32.6–32.8 eV [25,26]. Considering this location, this peak was identified as W-C bonding. The second peak located at a BE of 32.6 ± 0.1 eV originates from W-S bonds in WS_2. The peak located at 33.6 ± 0.2 eV is associated with W-O bonds in a sub-stoichiometric WO_x compound. The final doublet with the $W4f_{7/2}$ location at 35.6 ± 0.1 eV is in excellent agreement with the reference values for WO_3 [23,24,26,27], which also indicates that the charge correction method is appropriate. A single peak was also used at BE 37–38 eV, which represents the $W5p_{3/2}$ peak. Spectra obtained after sputter cleaning were fitted using three doublets. The main doublets are shifted towards lower binding energies compared to the spectra obtained before sputter cleaning. The location of the first doublet is at a BE of 31.7 ± 0.1 eV, which is in the typical range (31.5–32 eV) for W-C bonds presented in the literature [17,18,22]; the identification of C-W bonds in the C1s spectra confirms the identification of the W-C bonding from the W4f spectrum obtained after sputter cleaning. The second doublet at a higher binding energy of 32.1 ± 0.1 eV was identified as W-S bonds in a sub-stoichiometric WS_x compound. A shift towards a lower binding energy of the W4f peak representing W-S bonding is expected, which is a result of preferential sputtering of the chalcogen atom (S in this case) during sputter cleaning of the samples [28]. The third doublet added at a BE of 33-33.2 eV represents W-O bonding in WO_2. To finalize the fitting, a broad $W5p_{3/2}$ peak was added at a BE of 37–38 eV. The intensity of the third doublet might be exaggerated as the fitting of W-S bonding and W-C bonding is performed by asymmetric lineshapes, with asymmetry towards higher binding energy. As a result of the interaction between the core-hole and conduction electrons, XPS core level spectra of metals are often fitted with asymmetric lineshapes, with pronounced asymmetry towards higher binding energies (e.g., Doniach–Sunjic lineshape) [23,29–31]. In a recent XPS study on tungsten carbide nanopowders, Krasovskii et al. [23] reached a good fit on W4f core-level spectra using asymmetric lineshapes representative of W-C bonds, with asymmetry towards higher binding energy. The high-resolution core-level W4f XPS spectra of WS_2 powder performed by Morgan [25] were also fitted using asymmetric lineshapes representative of W-S bonding. The introduction of asymmetric lineshapes for fitting the spectra will significantly increase the complexity of the fitting procedure because of the additional fitting parameters; therefore, fitting was performed using symmetric Gaussian–Lorentzian lineshapes.

Representative spectra from the D3-17 coating, before and after etching, in the S2p region of interest are shown in Figure 6. Fitting was done using 1.18 eV separation for the $S2p_{3/2}$- $S2p_{1/2}$ doublet, with their peak area ratios set to 2. Spectra acquired before etching were fitted with three doublets. The first doublet located at a lower binding energy with a BE location of 161.6 ± 0.1 eV was at the location typical for sulfide ions (S^{2-}) originating from a sub-stoichiometric WS_x compound [26,32]. A second smaller doublet was added at $S2p_{3/2}$ BE energy of 162.2–162.5 eV, at a location representing disulfide ions (S_2^{2-}) originating from WS_2 [25,26,33]. To finalize the fitting, a doublet at a higher binding energy (163.4 ± 0.1 eV) was introduced, related to S-S bonding [33,34]. In an XPS study on WS_2 thin films, Zabinski et al. [33] also observed intensities at higher binding energy in S2p spectra, which the authors correlated with elemental sulfur condensed on the surfaces after deposition. Sulfur with high vapor pressure can be still present in the chamber even after discharge is stopped, resulting in subsequent condensation on the substrates. S2p spectra acquired after etching were fitted in a similar manner to the spectra acquired before etching, the differences being the usage of only two doublets in some of the spectra (see Figure 6b) and a reduction of the intensity in the higher binding energy portion of the spectra. Considering that the intensity at high binding energy is reduced, it is likely that there is condensation of residual sulfur present in the chamber after the discharge at the cathodes is stopped.

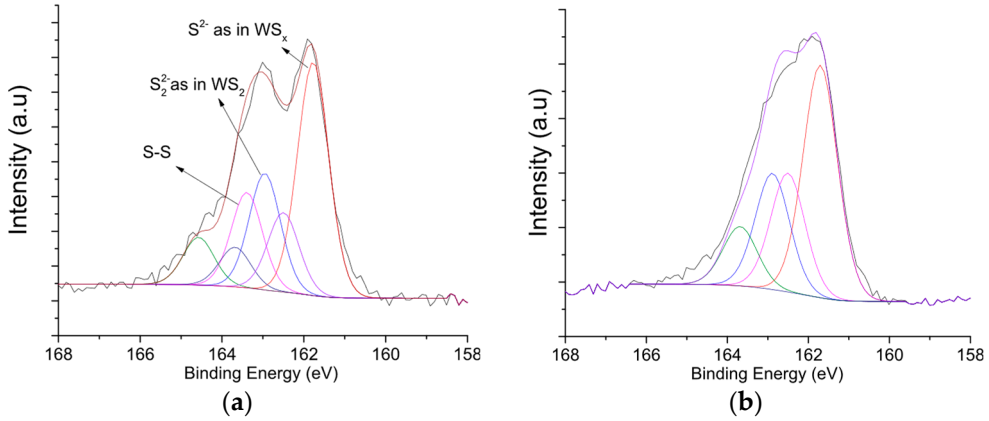

Figure 6. XPS spectra obtained in the S2p region of interest: (**a**) D3-17 before etching; (**b**) D3-17 after etching.

Raman spectra of selected coatings representing each route of deposition in the range 100–2000 cm^{-1} are presented in Figure 7. Magnetron-sputtered TMD-C films generally have two regions, with features representing different phases present in the film. The first region at Raman shift values of 300-450 cm represents the presence of the TMD phase. For WS_2, there are two distinct peaks. The peak at 350 cm^{-1} is related to the in-plane phonon mode $E^1{}_{2g}(\Gamma)$, while the peak at 412 cm^{-1} represents the out-of-plane phonon mode $A_{1g}(\Gamma)$ [35]. Distinct peaks related to the WS_2 phase can be observed for the D2-17 coatings. These features are in agreement with the XRD results. The coatings with higher carbon contents (representative spectra are shown from the D1-450 and D4-38 coatings) showed more featureless spectra in the WS_2 region of interest, confirming the poor crystallinity of the WS_2 phase.

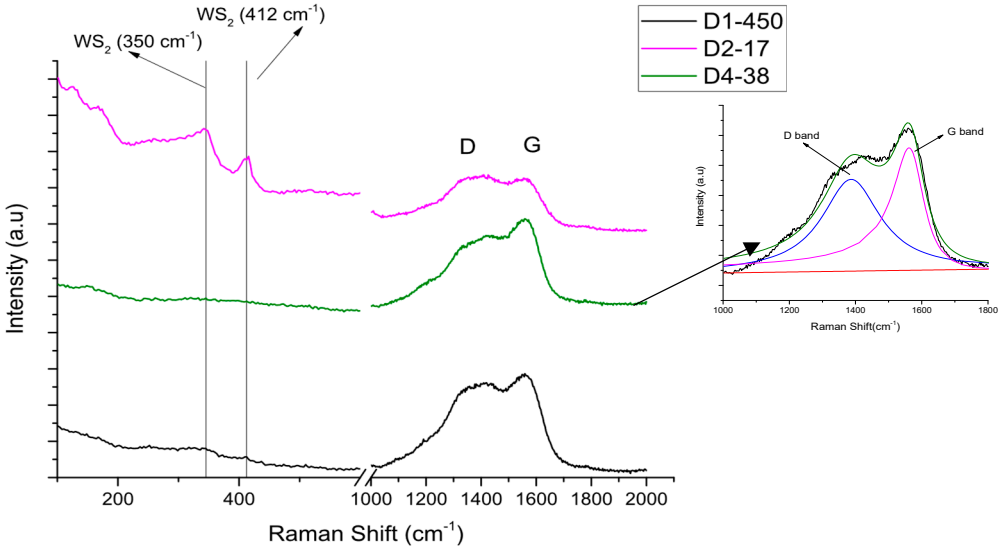

Figure 7. Raman spectra acquired from representative coatings.

The second region between 1100 and 1800 cm^{-1} contains the D and G bands of carbon. These peaks were fitted using a Breit–Wigner–Fano lineshape for the G peak and a Lorentzian lineshape for the D peak, as proposed by Ferrari et al. [36]. The fitting resulted in the ratios of the intensity of the D and G peaks (I_D/I_G) having values in the range 0.8–1.1. The location of the G band was typically below 1580 cm^{-1}. Considering these values and according to the four-stage model proposed by Ferrari et al., the carbon phase is in the second stage where it is present as amorphous carbon with predominant sp^2 bonds and a minor presence of sp^3 bonds.

3.3. Mechanical Properties

The hardness results from nanoindentation experiments are shown in Figure 8. The horizontal axis shows the power to the carbon target, the number of pellets used for deposition, or the partial pressure of the CH_4 gas, depending on the deposition procedure.

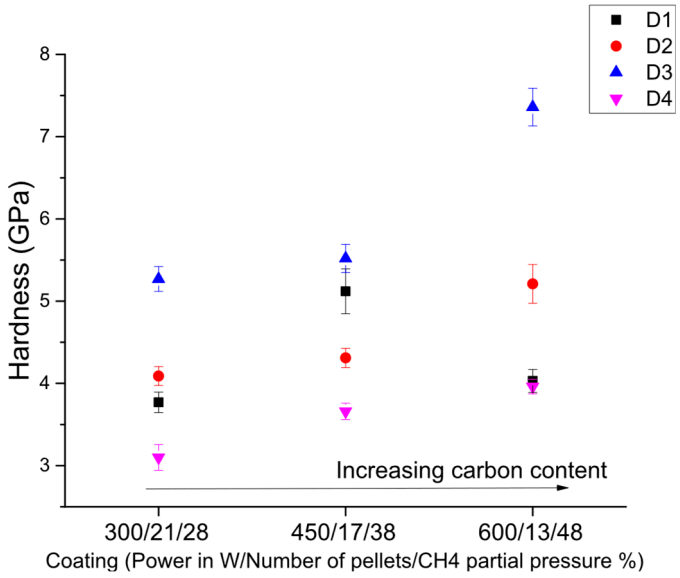

Figure 8. Hardness of the coatings.

The highest hardness was measured for the coatings deposited by sputtering a composite target in stationary mode (D3), followed by the films deposited by co-sputtering (D1), and sputtering a composite target in intermittent mode (D2). The coatings deposited in reactive mode generally showed lower hardness. The D3 coatings are harder compared to the D1 coatings, although they contain lesser amounts of carbon. The higher hardness is very likely because of the lower S/W ratio, which can be indicative of increased amounts of harder WC inclusions. The increased presence of WC is further supported by the higher peak area ratio between the C-W and C-C peaks in the C1s spectra for the D3 coatings as compared to the D1 ones (for example, compare Figures 4e and 4a). Additionally, these coatings deposited with the stationary holder in front of the target are subjected to higher bombardment with reflected Ar neutrals. In this context, it is expected that these coatings are more compact and hence harder. The lower hardness observed for the reactively sputtered coatings can be related to the hydrogenation of the a-C phase, as hydrogenated carbon coatings are often softer compared to their hydrogen-free counterparts [37]. The hardness values generally follow increasing trends in relation to C content, except for the co-sputtered coating (D1-600) with the highest C content (~48 at.%), which has a lower value compared to the coating with 42 at.% C (D1-450). The presence of higher C contents improves the compactness of the coatings, resulting in higher hardness. A pure carbon coating deposited using the same equipment has a hardness of ~8 GPa [38]. The higher hardness of D1-450 compared to its counterpart (D1-600) with a higher C content can be associated with the lower S/W ratio observed for this coating. The lower S/W ratio can be related to an increased presence of harder WC inclusions.

Scratch scar optical micrographs are shown in Figure 9. A single scar from each deposition route is shown because the features observed were quite similar between coatings deposited by the same deposition route. The results associated with critical load are presented in Table 2. Lc1 corresponds to the first appearance of cracks on the edge of the scratch scar. The critical load of the Lc_2 type corresponds to the first delamination (chipping) occurring on the sides of the scratch scar, while the Lc_3 critical load is the load at which the coating is totally removed from the surface [39]. Coatings of D1 and D2 types showed adhesion failures with Lc_3 critical loads of 14 N (for D1-450) and 13 N

(for D2-17). Lc_1 and Lc_2 loads were not detected (no cracking or chipping on the sides of the scar was observed) in these cases. As soon as the loads of 13–14 N were achieved, gross spallation was observed. The failure mode for these coatings was identified as wedge spallation.

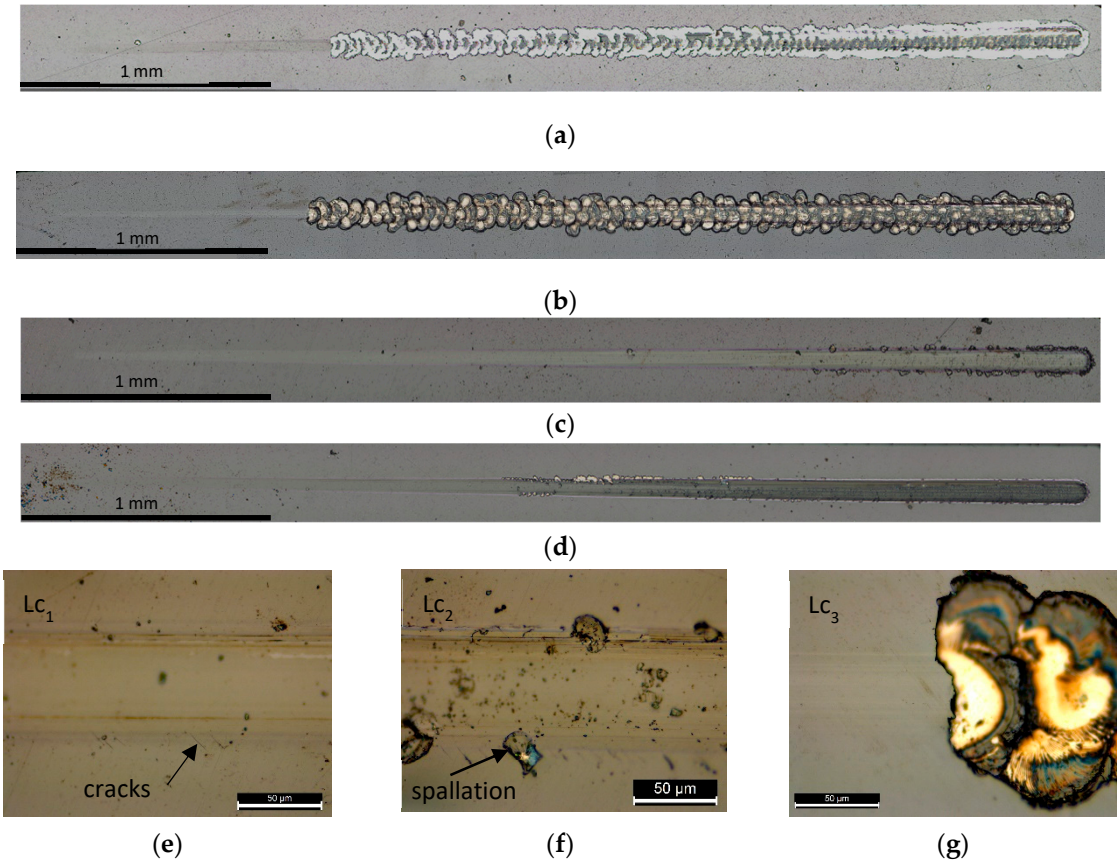

Figure 9. Scratch scars optical micrographs: (**a**) D1-450; (**b**) D2-17; (**c**) D3-17; (**d**) D4-38; (**e**) Lc1 detail acquired from the D3-17 scratch scar; (**f**) Lc2 detail from the D3-13 scar; (**g**) Lc3 detail from the D2-17 scar.

Table 2. Mechanical properties and adhesion of the coatings.

	Hardness [GPa]	Reduced Modulus [GPa]	Critical Load Lc_2 [N]	Critical Load Lc_2 [N]	Critical Load Lc_3 [N]
D1-300	3.77 ± 0.12	63.1 ± 1.3			19 ± 1
D1-450	5.12 ± 0.27	60 ± 1.6			14 ± 2
D1-600	4.03 ± 0.14	44.63 ± 1.2			13 ± 2
D2-21	4.09 ± 0.11	55.9 ± 2.1			7 ± 1
D2-17	4.31 ± 0.12	60.8 ± 1.1			13 ± 1
D2-13	5.21 ± 0.23	62.3 ± 1.4			7 ± 1
D3-21	5.27 ± 0.15	86 ± 1.6	12 ± 1	22 ± 1	>40
D3-17	5.52 ± 0.17	88 ± 1.2	21 ± 1	28 ± 3	>40
D3-13	7.36 ± 0.23	97 ± 2.6	16 ± 1	20 ± 1	>40
D4-28	3.1 ± 0.16	61.7 ± 2.7	11 ± 1	21 ± 1	>40
D4-38	3.66 ± 0.1	61 ± 1		20 ± 1	>40
D4-48	3.96 ± 0.09	84.3 ± 2		19 ± 1	>40

The D3 and D4 coatings showed improved adhesion. Cracking was observed for the D3 coatings as well as for the D4 coating deposited under the lowest partial pressure of CH_4. The Lc_1 loads were in the range of 12–19 N for the D3 coatings and ~11 N for the D4-28 coating. A representative detail regarding the cracking observed is shown in Figure 9e. The Lc_2 loads (a representative detail is shown in Figure 9f) were between 20 and 28 N for D3 coatings, and 19 and 21 N for the D4 ones. It should

be noted that no complete removal of the coating occurred in the current load range for the D3 and D4 coatings.

The deteriorated behavior for D1 coatings can be related to the inability to deposit an interlayer. Delamination of the coating from the substrate in this case is very likely due to the bonding type mismatch between the coating and the substrate. As for D2 coatings, the spallation is most probably due to the columnar morphology, which is more porous by nature, with the presence of columnar boundaries. The presence of columnar boundaries is unfavorable in terms of crack initiation and propagation and, hence, the films are more prone to spallation. The improved behavior for D3 and D4 films is associated with the compact featureless morphology and the presence of the Cr interlayer.

3.4. Tribological Properties

Results from the tribological tests are shown in Figure 10. A coating with intermediate carbon content was selected from each deposition process.

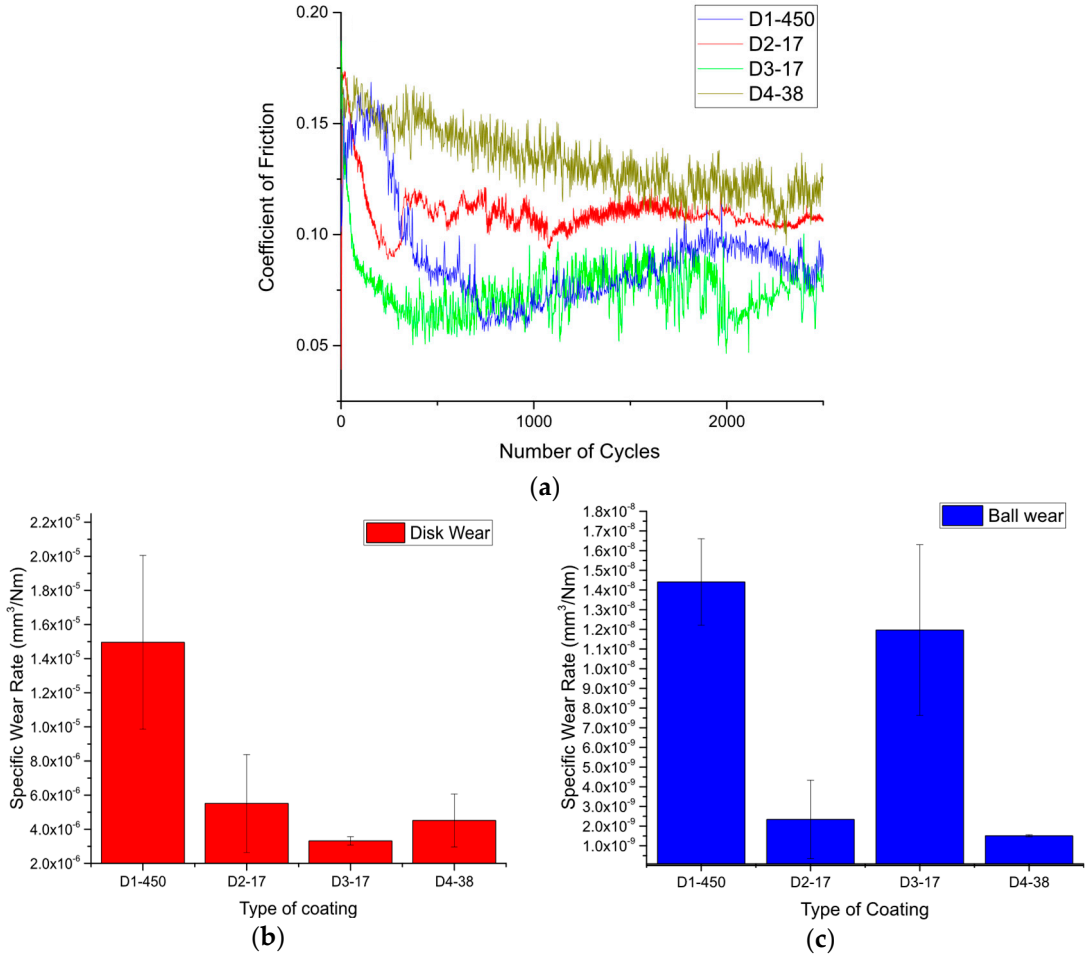

Figure 10. Tribological properties of selected coatings: (**a**) friction coefficient; (**b**) specific wear rate of the coated disks; (**c**) specific wear rate of the balls.

The coating deposited by co-sputtering (D1-450) shows a steady running-in period with a drop of friction coefficient to ~0.06 at ~800 cycles; furthermore, fluctuations at values around 0.06–0.08 were observed for ~500 cycles, followed by an increase in friction, indicating potential failure of the coating. The 2D profilometry shows wear depths of ~1.5 µm, a value which is close to the thickness of the coating. The optical micrograph obtained for the wear scars shows large delaminated areas. The wear rate of the coating was the highest, with a value of 1.5×10^{-5} mm^3/Nm. The drop of the friction down to 0.06 indicates the presence of a TMD tribofilm at the sliding interface, but the

inability to deposit an interlayer was probably crucial as rapid wear of the coating occurs, which can be related to poor adhesion of the coating (large delaminated areas are observed on the wear scar). The behavior of the D2-17 coating is slightly different, with a short running-in period, after which the friction coefficient drops to 0.09–0.1, followed by a small increase and stabilization of the friction coefficient at a value of ~0.11–0.12. The specific wear rate was ~ 5×10^{-6} mm^3/Nm, a much better value compared to the D1-450 coating. The optical micrograph (see Figure 11c) shows areas on the wear scars in which the coating is worn through, but not to the same extent as the D1-450 coating. The coating D3-17 shows the best performance as the coefficient of friction was quite low, dropping to ~0.06 in the first ~700 cycles, with fluctuations between 0.06 and 0.08 for the remaining time of the test. This coating also outperformed the other coatings in terms of wear resistance, with a specific wear rate of 3×10^{-6} mm^3/Nm. The optical micrograph (Figure 11e) of the wear scar does not show any signs of delamination. The reactive sputtered coating (D4-38) had a higher friction coefficient compared to the other coatings, with a starting value of 0.16, a value that steadily dropped to ~0.12 by the end of the duration of the test. The integrity of the coating was preserved during testing (see Figure 11g), with a specific wear rate of ~ 4×10^{-6} mm^3/Nm.

In terms of ball wear, higher values were observed for the D1 and D3 coatings (~ 1×10^{-8} mm^3/Nm). The higher wear for the ball counterpart sliding against the D1 coating is very likely due to the increased interaction of the ball with the harder steel counterpart, further resulting in generation of an iron-rich third body, which can cause third body abrasion. This process will result in an increased coefficient of friction as the iron rich debris does not possess low shear strength. As for the ball sliding against the D3 coating, the increased wear may be due to the increased hardness of the D3 coating. The harder D3-17 coating most probably contains more WC inclusions, which are very hard and can cause abrasive wear on the steel counterpart. In the case of the D2 and D4 coatings, the formation of a protective transfer film results in reduced wear of the counterbody.

Considering the low value observed for the friction coefficient (~0.06–0.08) in the D1-450 and D3-17 coatings, it can be assumed that the friction is at least partially governed by a WS_2 phase. It should be noted that pure carbon films deposited using the same equipment, sliding against a steel counterbody, under similar conditions, show a coefficient of friction of ~0.2 (see Ref. [40]). The D2-17 coatings, despite having a significant amount of WS_2, showed a higher coefficient of friction, which may be related to the partial interaction between the steel counterbody and the steel disk due to the presence of areas on the wear track where the W-S-C coating was delaminated. In the case of the reactively sputtered coatings, the friction was slightly higher, but stable. Considering the high amount of C contained in the coating, and the higher overall friction coefficient, it is very likely that the carbon phase plays the main role in governing the friction.

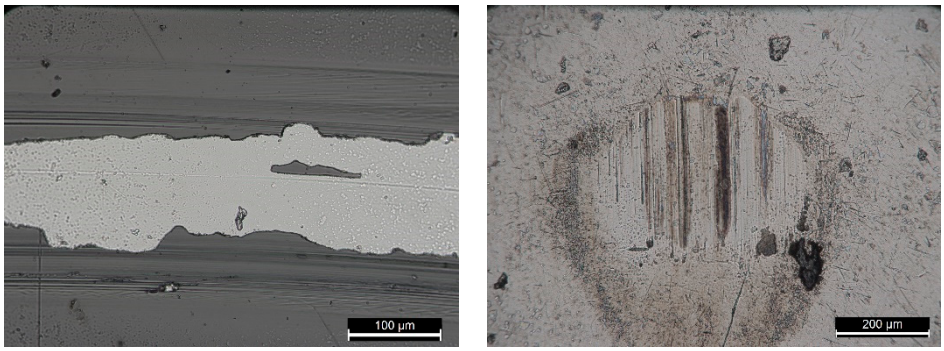

(**a**) (**b**)

Figure 11. *Cont.*

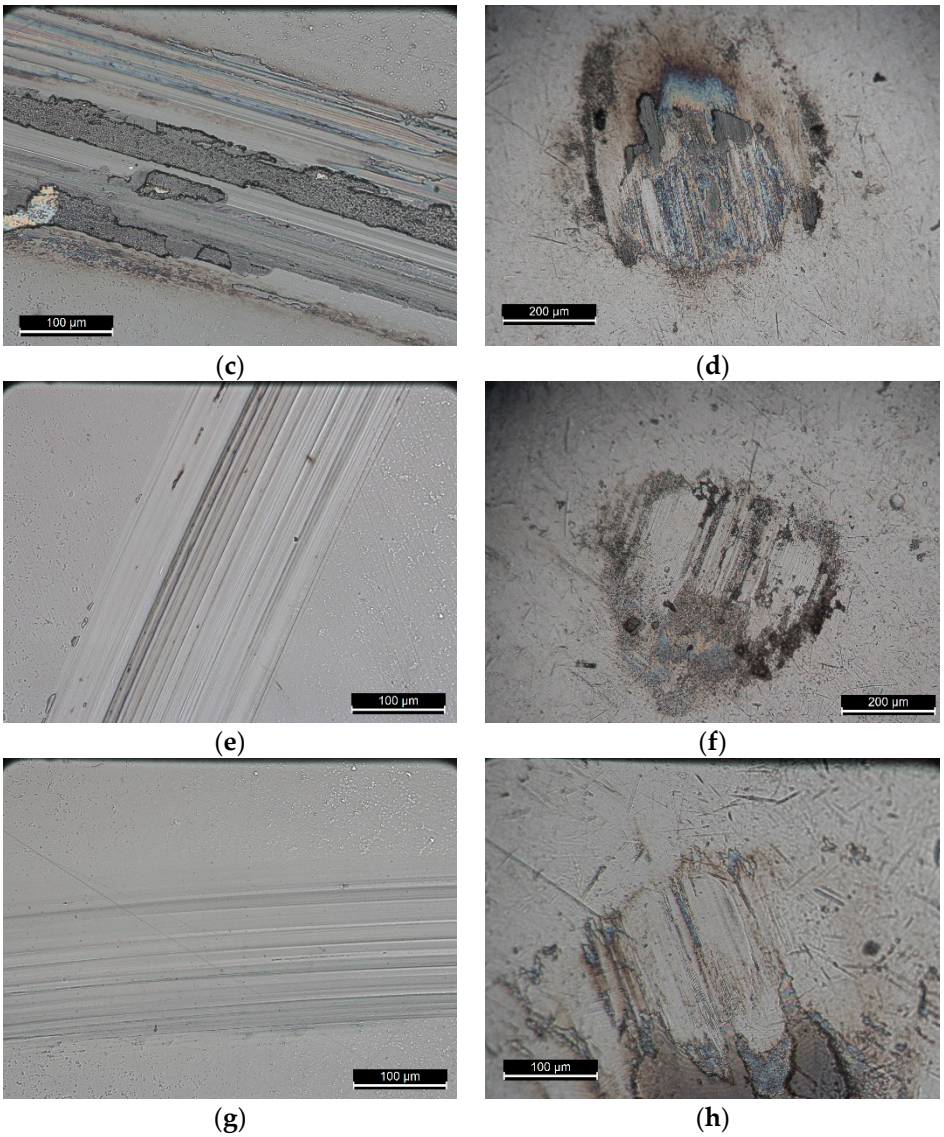

Figure 11. Optical micrographs of the wear tracks on the disk and the wear scars on counterbodies: (**a**) D1-450 disk; (**b**) D1-450 ball; (**c**) D2-17 disk; (**d**) D2-17 ball; (**e**) D3-17-disk; (**f**) D3-17-ball; (**g**) D4-38 disk; (**h**) D4-38 ball.

In summary, the best performance was observed for the coating deposited by sputtering a composite target with the substrate holder being stationary (D3). Its good performance may be related to the compact morphology resulting from the optimal carbon content and a suitable S/W ratio. Moreover, the coating responded well to scratch testing, with the highest value of the Lc2 load and no gross delamination.

4. Conclusions

W-S-C(H) coatings were deposited by RF magnetron sputtering using four different procedures. The chemical composition of the coatings varied depending on the power used on the targets, the number of pellets used, and the partial pressure of the CH_4 gas. The S/W ratio was the lowest for the reactively sputtered coatings and the coatings deposited by sputtering a composite target with the substrate being stationary. The difference in the S/W ratio was attributed to the different levels of bombardment with backscattered Ar neutrals. Cross-sectional micrographs showed dense and featureless morphologies, except for the films with low C contents, where columnar growth was observed. In terms of crystallinity, only the coatings with low C contents (<30 at.%) and high overall

amounts of S (>35 at.%) showed well-defined peaks related to planes of WS_2. The coatings with higher C contents (>30%) or low amounts of S (<30 at.%) had an X-ray diffraction amorphous structure, with the diffractograms showing a broad peak at 2θ = 33–50°. The XPS study revealed the presence of W-S and W-C bonds, in addition to C-C bonding. Raman spectroscopy revealed the presence of WS_2 crystals for the coatings with the highest amounts of S. The presence of a-C was also confirmed, since the location and intensity of the D and G peaks was in the typical range for a-C. The hardness of the coatings increased as the amount of C increased and the S/W ratio decreased. The hardness increase was attributed to the increased presence of a harder a-C phase, the existence of a W-C phase, and overall densification of the coatings. Reactive-sputtered coatings showed the lowest hardness. The introduction of a Cr interlayer proved to be crucial for the adhesion, since the coatings with the best adhesion where those where Cr interlayer was deposited. The tribological properties were related to the composition of the coatings as well as the overall mechanical properties. A coefficient of friction as low as ~0.06 could be achieved during dry sliding in ambient air for the hydrogen-free coatings with compact morphology and a C content of ~40 at.%.

For the upscaling of the W-S-C coatings, magnetron sputtering in non-reactive mode should be considered. Sputtering of a composite target (C with WS_2 pellets) and co-sputtering of individual WS_2 and C targets have the potential for providing tribologically viable coatings. To obtain compact morphologies with good mechanical properties, C contents should be higher than 30 at.%. The S/W ratio should be assessed carefully, as it can provide valuable information regarding the properties of the coatings. Deposition of a metallic interlayer should be performed in order to improve the adhesion of the coatings on metallic substrates.

Author Contributions: Conceptualization, T.V. and A.C.; Investigation, T.V. and T.B.Y.; Data curation, T.V. and T.B.Y.; Funding acquisition, A.C.; Project administration, A.C.; Supervision, M.E. and A.C.; Visualization, T.V. and T.B.Y.; Writing—original draft preparation, T.V.; Writing—review and editing, M.E. and A.C. All authors have read and agreed to the published version of the manuscript.

Funding: This project received funding from the European Union's Horizon 2020 research and innovation programme under grant agreement No. 721642: SOLUTION.

Acknowledgments: The authors would also like to acknowledge financial support from the projects: ATRITO-0 [co-financed via FEDER (PT2020) POCI-01-0145-FEDER-030446 and FCT (PIDDAC)], On-SURF [co-financed via FEDER (PT2020) POCI-01-0247-FEDER-024521] and CEMMPRE—UID/EMS/00285/2020 [co-financed via FEDER and FCT (COMPETE)].

Conflicts of Interest: The authors declare no conflicts of interest.

References

1. Prasad, S.; Zabinski, J. Super slippery solids. *Nature* **1997**, *387*, 761. [CrossRef]
2. Voevodin, A.A.; O'Neill, J.P.; Zabinski, J.S. Nanocomposite tribological coatings for aerospace applications. *Surf. Coat. Technol.* **1999**, *116*, 36–45. [CrossRef]
3. Kalin, M.; Kogovšek, J.; Remškar, M. Mechanisms and improvements in the friction and wear behavior using MoS_2 nanotubes as potential oil additives. *Wear* **2012**, *280*, 36–45. [CrossRef]
4. Kosarieh, S.; Morina, A.; Lainé, E.; Flemming, J.; Neville, A. The effect of MoDTC-type friction modifier on the wear performance of a hydrogenated DLC coating. *Wear* **2013**, *302*, 890–898. [CrossRef]
5. Teer, D.G.; Hampshire, J.; Fox, V.; Bellido-Gonzalez, V. The tribological properties of MoS_2/metal composite coatings deposited by closed field magnetron sputtering. *Surf. Coat. Technol.* **1997**, *94*, 572–577. [CrossRef]
6. Deepthi, B.; Barshilia, H.C.; Rajam, K.S.; Konchady, M.S.; Pai, D.M.; Sankar, J. Mechanical and tribological properties of sputter deposited nanostructured Cr–WS_2 solid lubricant coatings. *Surf. Coat. Technol.* **2010**, *205*, 1937–1946. [CrossRef]
7. Nossa, A.; Cavaleiro, A. Chemical and physical characterization of C(N)-doped W-S sputtered films. *J. Mater. Res.* **2004**, *19*, 2356–2365. [CrossRef]
8. Vuchkov, T.; Evaristo, M.; Yaqub, T.B.; Cavaleiro, A. The effect of substrate location on the composition, microstructure and mechano-tribological properties of W-S-C coatings deposited by magnetron sputtering. *Surf. Coat. Technol.* **2020**, 125481. [CrossRef]

9. Scharf, T.W.; Kotula, P.G.; Prasad, S.V. Friction and wear mechanisms in MoS_2/Sb_2O_3/Au nanocomposite coatings. *Acta Mater.* **2010**, *58*, 4100–4109. [CrossRef]
10. Polcar, T.; Cavaleiro, A. Review on self-lubricant transition metal dichalcogenide nanocomposite coatings alloyed with carbon. *Surf. Coat. Technol.* **2011**, *206*, 686–695. [CrossRef]
11. Voevodin, A.A.; Zabinski, J.S. Supertough wear-resistant coatings with "chameleon" surface adaptation. *Thin Solid Films* **2000**, *370*, 223–231. [CrossRef]
12. Polcar, T.; Cavaleiro, A. Self-adaptive low friction coatings based on transition metal dichalcogenides. *Thin Solid Films* **2011**, *519*, 4037–4044. [CrossRef]
13. Cao, H.; Wen, F.; Kumar, S.; Rudolf, P.; de Hosson, J.T.M.; Pei, Y. On the S/W stoichiometry and triboperformance of WSxC(H) coatings deposited by magnetron sputtering. *Surf. Coat. Technol.* **2018**. [CrossRef]
14. Evaristo, M.; Nossa, A.; Cavaleiro, A. W–S–C sputtered films: Influence of the carbon alloying method on the mechanical properties. *Surf. Coat. Technol.* **2005**, *200*, 1076–1079. [CrossRef]
15. Evaristo, M.; Polcar, T.; Cavaleiro, A. Can {W-Se-C} Coatings Be Competitive to {W-S-C} Ones? *Plasma Process. Polym.* **2009**, *6*, S92–S95. [CrossRef]
16. Nossa, A.; Cavaleiro, A. Mechanical behaviour of W-S-N and W-S-C sputtered coatings deposited with a Ti interlayer. *Surf. Coat. Technol.* **2003**, *163*, 552–560. [CrossRef]
17. Voevodin, A.A.; Fitz, T.A.; Hu, J.J.; Zabinski, J.S. Nanocomposite tribological coatings with "chameleon" surface adaptation. *J. Vac. Sci. Technol. A Vac. Surf. Film* **2002**, *20*, 1434–1444. [CrossRef]
18. Särhammar, E.; Strandberg, E.; Sundberg, J.; Nyberg, H.; Kubart, T.; Jacobson, S.; Jansson, U.; Nyberg, T. Mechanisms for compositional variations of coatings sputtered from a WS_2 target. *Surf. Coat. Technol.* **2014**, *252*, 186–190. [CrossRef]
19. Petrov, I.; Barna, P.B.; Hultman, L.; Greene, J.E. Microstructural evolution during film growth. *J. Vac. Sci. Technol. A Vac. Surf. Film* **2003**, *21*, S117–S128. [CrossRef]
20. Weise, G.; Mattern, N.; Hermann, H.; Teresiak, A.; Ba, I.; Bru, W. Preparation, structure and properties of MoS x films. *Thin Solid Films* **1997**, *298*, 98–106. [CrossRef]
21. Voevodin, A.A.; O'Neill, J.P.; Prasad, S.V.; Zabinski, J.S. Nanocrystalline WC and WC/a-C composite coatings produced from intersected plasma fluxes at low deposition temperatures. *J. Vac. Sci. Technol. A Vac. Surf. Film* **1999**, *17*, 986–992. [CrossRef]
22. Abad, M.D.; Muñoz-Márquez, M.A.; el Mrabet, S.; Justo, A.; Sánchez-López, J.C. Tailored synthesis of nanostructured WC/a-C coatings by dual magnetron sputtering. *Surf. Coat. Technol.* **2010**, *204*, 3490–3500. [CrossRef]
23. Krasovskii, P.V.; Malinovskaya, O.S.; Samokhin, A.V.; Blagoveshchenskiy, Y.V.; Kazakov, V.A.; Ashmarin, A.A. XPS study of surface chemistry of tungsten carbides nanopowders produced through DC thermal plasma/hydrogen annealing process. *Appl. Surf. Sci.* **2015**, *339*, 46–54. [CrossRef]
24. Moulder, J.F.; Chastain, J. Handbook of x-ray photoelectron spectroscopy: A reference book of standard spectra for identification and interpretation of XPS data. *Phys. Electron. Div. Perkin Elmer Corp* **1992**, *40*, 221. Available online: https://books.google.pt/books/about/Handbook_of_X_ray_Photoelectron_Spectros.html?id=A_XGQgAACAAJ&redir_esc=y (accessed on 14 January 2019).
25. Morgan, D.J. Core-level spectra of powdered tungsten disulfide, WS_2. *Surf. Sci. Spectra.* **2018**, *25*, 14002. [CrossRef]
26. Martin-Litas, I.; Vinatier, P.; Levasseur, A.; Dupin, J.; Gonbeau, D.; Weill, F. Characterisation of r.f. sputtered tungsten disulfide and oxysulfide thin films. *Thin Solid Films* **2002**, *416*, 1–9. [CrossRef]
27. Dupin, J.-C.; Gonbeau, D.; Vinatier, P.; Levasseur, A. Systematic XPS studies of metal oxides, hydroxides and peroxides. *Phys. Chem. Chem. Phys.* **2000**, *2*, 1319–1324. [CrossRef]
28. Bernède, J. About the preferential sputtering of chalcogen from transition metal dichalcogenide compounds and the determination of compound stoichiometry from XPS peak positions. *Appl. Surf. Sci.* **2001**, *171*, 15–20. [CrossRef]
29. Doniach, S.; Sunjic, M. Many-electron singularity in X-ray photoemission and X-ray line spectra from metals. *J. Phys. C Solid State Phys.* **1970**, *3*, 285–291. [CrossRef]
30. Hüfner, S. *Continuous Satellites and Plasmon Satellites: XPS Photoemission in Nearly Free Electron Systems*; Springer: Berlin/Heidelberg, Germany, 2003; pp. 173–209. [CrossRef]

31. Shevchik, N.J. Physical Review Letters Local Density of States and Core-Hole Conduction-Electron Interactions in the X-Ray Photoemission Spectra of Pt and Ni. *Phys. Rev. Lett.* **1974**, *33*, 1336. Available online: https://journals.aps.org/prl/pdf/10.1103/PhysRevLett.33.1336 (accessed on 25 January 2019). [CrossRef]
32. Smart, R.S.C.; Skinner, W.M.; Gerson, A.R. XPS of sulphide mineral surfaces: Metal-deficient, polysulphides, defects and elemental sulphur. *Surf. Interface Anal.* **1999**, *28*, 101–105. [CrossRef]
33. Zabinski, J.S.; Donley, M.S.; Prasad, S.V.; Mcdevitt, N.T. Synthesis and characterization of tungsten disulphide films grown by pulsed-laser deposition. *J. Mater. Sci.* **1994**, *29*, 4834–4839. Available online: https://link.springer.com/content/pdf/10.1007/BF00356530.pdf (accessed on 25 January 2019). [CrossRef]
34. Wang, Z.; Dong, Y.; Li, H.; Zhao, Z.; Wu, H.B.; Hao, C.; Liu, S.; Qiu, J.; Lou, X.W. Enhancing lithium–sulphur battery performance by strongly binding the discharge products on amino-functionalized reduced graphene oxide. *Nat. Commun.* **2014**, *5*, 6002. [CrossRef] [PubMed]
35. Berkdemir, A.; Gutiérrez, H.R.; Botello-Méndez, A.R.; Perea-López, N.; Elías, A.L.; Chia, C.-I.; Wang, B.; Crespi, V.H.; López-Urías, F.; Charlier, J.-C.; et al. Identification of individual and few layers of WS_2 using Raman Spectroscopy. *Sci. Rep.* **2013**, *3*, 1755. [CrossRef]
36. Ferrari, A.C.; Robertson, J. Interpretation of Raman spectra of disordered and amorphous carbon. *Phys. Rev. B* **2000**, *61*, 14095–14107. [CrossRef]
37. Donnet, C.; Erdemir, A. *Diamond-Like Carbon Films: A Historical Overview*; Springer: Berlin/Heidelberg, Germany, 2008. [CrossRef]
38. Polcar, T.; Evaristo, M.; Cavaleiro, A. Friction of Self-Lubricating W-S-C Sputtered Coatings Sliding under Increasing Load. *Plasma Process. Polym.* **2007**, *4*, S541–S546. [CrossRef]
39. Stallard, J.; Poulat, S.; Teer, D.G. The study of the adhesion of a TiN coating on steel and titanium alloy substrates using a multi-mode scratch tester. *Tribol. Int.* **2006**, *39*, 159–166. [CrossRef]
40. e Silva, C.W.M.; Branco, J.R.T.; Cavaleiro, A. How can H content influence the tribological behaviour of W-containing DLC coatings. *Solid State Sci.* **2009**, *11*, 1778–1782. [CrossRef]